

High pressure single-crystal micro X-ray diffraction analysis with GSE_ADA/RSV software

Przemyslaw Dera^{a,b,*}, Kirill Zhuravlev^a, Vitali Prakapenka^a, Mark L. Rivers^a, Gregory J. Finkelstein^c, Ognjen Grubor-Urosevic^d, Oliver Tschauner^d, Simon M. Clark^e and Robert T. Downs^f

^aCenter for Advanced Radiation Sources, Argonne National Laboratory, University of Chicago, Argonne, IL, USA; ^bSchool of Ocean and Earth Science and Technology, Hawaii Institute of Geophysics and Planetology, University of Hawaii at Manoa, Honolulu, HI, USA; ^cDepartment of Geosciences, Princeton University, Princeton, NJ, USA; ^dHigh Pressure Science and Technology Center, University of Nevada at Las Vegas, Las Vegas, NV, USA; ^eDepartment of Earth and Planetary Sciences, Macquarie University, North Ryde, Australia; ^fGeology Department, University of Arizona, Tucson, AZ, USA

(Received 25 April 2013; final version received 11 May 2013)

GSE_ADA/RSV is a free software package for custom analysis of single-crystal micro X-ray diffraction (SC μ XRD) data, developed with particular emphasis on data from samples enclosed in diamond anvil cells and subject to high pressure conditions. The package has been in extensive use at the high pressure beamlines of Advanced Photon Source (APS), Argonne National Laboratory and Advanced Light Source (ALS), Lawrence Berkeley National Laboratory. The software is optimized for processing of wide-rotation images and includes a variety of peak intensity corrections and peak filtering features, which are custom-designed to make processing of high pressure SC μ XRD easier and more reliable.

Keywords: single-crystal X-ray diffraction; high pressure; diamond anvil cell; area detectors

1. Introduction

GSE_ADA and Reciprocal Space Viewer (RSV) are two distinct computer programs written in the Interactive Data Language (IDL) and custom-designed for analysis of single-crystal micro X-ray diffraction (SC μ XRD) data collected from samples enclosed in diamond anvil cells (DACs). The first paper reporting the use of GSE_ADA and RSV for analysis of SC μ XRD data was published in 2008.[1] To date 23 papers utilizing GSE_ADA and RSV have been published or submitted.[1–23] The fields of application of the software range from mineral physics,[1–3,5,7–9,14,15,17–22] through chemistry and materials science [6,12,23] to condensed matter physics.[4,10,11,16]

High pressure crystallographic data differ from data collected at ambient conditions in several important ways: (a) the diffraction signal from the sample is contaminated by contributions from parts of the DAC such as the two single-crystal diamond anvils, backing plates, pressure transmitting medium, gasket, etc. (b) the coverage of reciprocal space is limited because of the restricted angular access to the sample, and (c) the quality of the sample crystals (*e.g.* mosaicity) is often

*Corresponding author. Email: pdera@hawaii.edu

low as a result of the presence of nonhydrostatic stress. Several comprehensive overviews of the intricacies of high pressure crystallographic experiments have been published [24–27] and it is not the intention of this paper to systematically review all of the previously discussed material. Instead, we will focus on the most relevant aspects of synchrotron experiments, with emphasis on customizations of the data collection, data analysis flow, and unique features of GSE_ADA/RSV, hoping to provide a convenient reference for the current and future users of the software, and to document the progress of high pressure experimental techniques.

1.1. Distribution

The GSE_ADA/RSV software is available for download from the following website: <https://sites.google.com/site/gseadawiki/home>.

The programs are distributed as IDL binaries (.sav), which can be executed with the use of the free IDL Virtual Machine.¹ The binary files are compatible with the IDL versions 6.4 and newer. The distribution website also provides access to an executable Windows installer program and some demonstration data. The screenshots of the GSE_ADA and RSV graphical user interfaces (GUIs) are shown in Figures 1 and 2.

1.2. Operating system compatibility

IDL is a multi-platform environment, compatible with common operating systems such as Microsoft Windows, Apple iOS and Linux. Currently, only 32-bit Windows binary files of GSE_ADA/RSV, compatible with IDL 6.4 and newer are available.

1.3. External IDL libraries, plugins and Windows dynamic link libraries

The IDL code of the GSE_ADA/RSV programs utilizes two external libraries, not included in the IDL distribution, MPFIT by Craig Markwardt² (nonlinear multi-parameter optimization) and

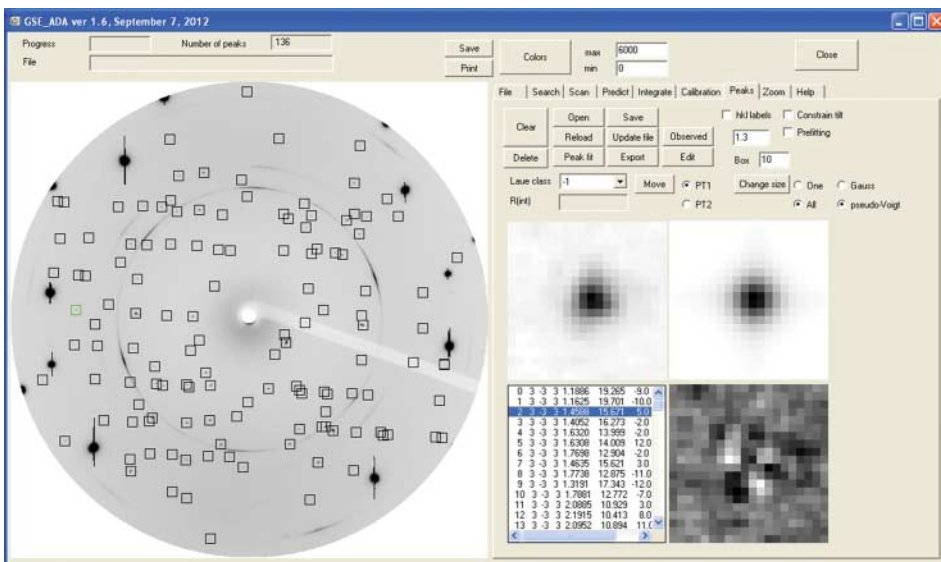


Figure 1. GUI of GSE_ADA version 1.6, showing the results of peak search (big image window on the left side) and two-dimensional peak fitting (three small image windows on the right side).

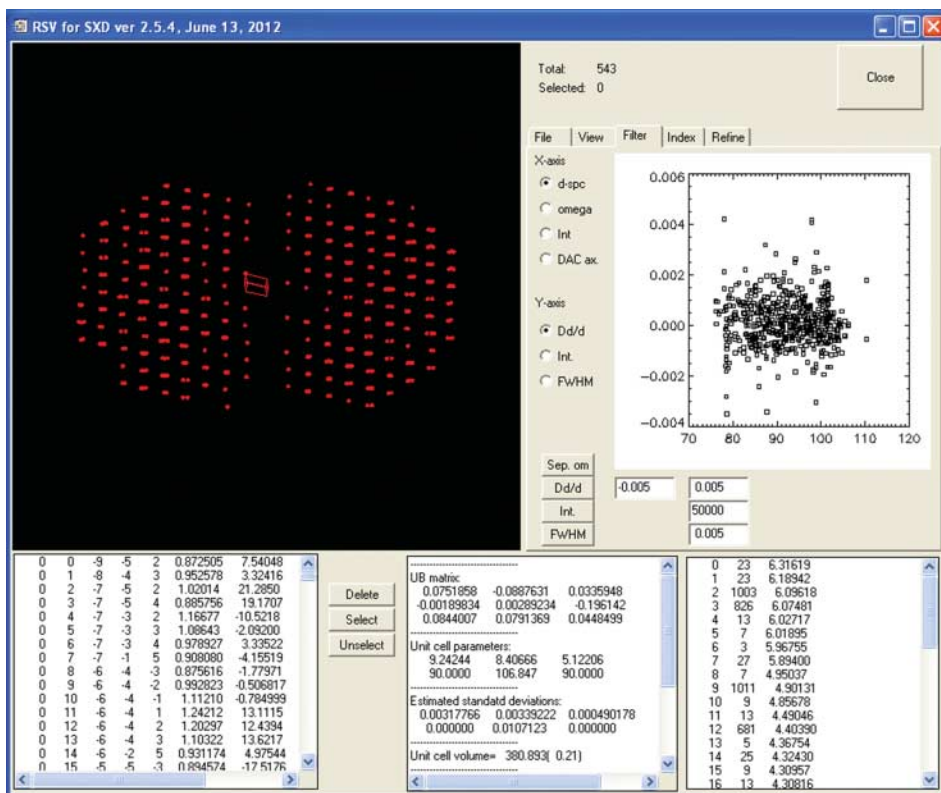


Figure 2. GUI of RSV ver. 2.5.4 showing projection of reciprocal space from the measurement on jadeite sample at 8.2(1) GPa, described in Section 4. Shown on the left side of the window is the d -spacing error analysis described in Section 3.6.

the Coyote library by David W. Fanning³ (some GUI and graphics/display elements). Both of these libraries are open-source.

RSV offers plugin access to two external programs: XPREP [28] for scaling, merging and space group determination, and CELL_NOW [29] for peak indexing and orientation matrix determination. The binaries of these two external programs are not distributed with GSE_ADA and responsibility for obtaining the necessary licenses rests with GSE_ADA users.

In order to speed up time-consuming tasks such as image integration and decompression of MAR345 format images, GSE_ADA uses two Windows dynamic link libraries MAR345_IDL.dll, written by Mark Rivers,⁴ and AD_Image8.dll, written by P. Dera. AD_Image8 was written and compiled using Embarcadero Delphi. At the moment this library is only available in a 32-bit Windows version. The functions controlled by the AD_Image8.dll library are currently not available for other than Windows operating systems.

2. Data collection strategies

2.1. Conventions

In the discussion that follows we use a reference coordinate system with x along the X-ray beam, z vertical, pointing upwards, and y in the horizontal plane of the instrument, completing a right-handed Cartesian basis. Positive and negative rotations are defined following the conventions

of Busing and Levy.[30] It should be noted that some beamline instruments define the positive rotations opposite to,[30] and may also use zero-positions for the goniometer rotations different than the conventional choice (*e.g.* for a two-axis ω - χ Eulerian goniometer the conventional zero of ω -axis should be defined such that it brings the χ circle to the plane normal to the incident beam and makes the χ -axis parallel to the beam, whereas at Sector 13, Advanced Photon Source (APS) such position is defined as $\omega = -90^\circ$). In these cases the necessity to convert the motor position reading to the conventional setting rests with the user.

2.2. DAC geometry and choice of backing plates

The most important difference between single-crystal and powder diffraction experiments with a DAC is the necessity for sample rotation in the former, to provide effective sampling of multiple diffraction events, which in general imposes a requirement of wider angular access to the sample. This requirement becomes critical for samples with lower symmetry and with small unit cells, as well as for acquiring good constraints on atomic displacement parameters. A consequence of restricted angular access may be that a data-set of measured reciprocal vectors becomes two-dimensional, making reliable data interpretation mathematically impossible. The angular access to the sample in a DAC is primarily determined by the diamond backing plates and height of the diamond anvil. Until recently, the majority of backing plates for single-crystal DACs were made of beryllium metal.[25] Be has a low absorption coefficient (0.033 mm^{-1} at 30 keV), which is particularly important for laboratory experiments with MoK α radiation ($E = 17.37 \text{ keV}$), for which absorption effects are more severe than at the typical energies $E > 30 \text{ keV}$ used at synchrotron beamlines. Placing the Be seat on the incident beam side allows rotation within the whole opening of the DAC ($\pm 45^\circ$ for the Merrill–Bassett DAC). For synchrotron SC μ XRD applications, however, Be plates are not very convenient because of the granularity of the Be metal, which produces very intense and spotty powder lines, significantly obscuring sample peaks (see *e.g.* [31,32]). Be is also not hard enough for experiments above 30 GPa, in which case plastic deformation occurs, leading to anvil misalignment, and ultimately failure. At ultra-high pressure Be plates also suffer from brittle fracture.

A preferred recent solution are diamond anvils with conical support surfaces, in Boehler–Almax (BA) geometry,[33] offering access to angles as large as $\pm 45^\circ$ without producing any powder diffraction signal from the backing plates. A popular alternative to BA diamonds are backing plates made of sintered cubic boron nitride (cBN). While having a relatively low absorption coefficient ($\sim 0.1 \text{ mm}^{-1}$ at 30 keV), with a height of $\sim 5 \text{ mm}$, the cBN seat absorbs the X-rays to a noticeable degree. A typical cBN plate has a conical access hole with an opening angle of about $\pm 15^\circ$. With the cBN seat used on the incident beam side of the DAC, the absorption of the beam changes rather dramatically with the sample rotation: from negligible, when the beam is passing through the conical opening, to about a factor of two, when the beam is passing through the full thickness of the seat. This absorption effect has to be corrected prior to using the measured peak intensities in structure determination. The correction procedure implemented in GSE_ADA is described in further detail in Section 3.8.3.

Unlike in powder diffraction studies, where the cBN seat is placed on the detector side of the DAC, in single-crystal experiments the cBN seats are used on the incident beam side (upstream) of the cell. The metal binder used for sintering during the manufacturing process produces a strong powder diffraction signal that contaminates the single-crystal diffraction images and makes peaks fitting and intensity extraction less reliable. If the cBN seat is on the detector side and the DAC is rotated beyond the opening of the seat access cone, this effect is unavoidable. Furthermore, strong diamond diffraction peaks traveling through the seat can cause secondary powder diffraction (Debye–Scherrer rings which are centered around the given diamond peak). A powder diffraction

signal is also created if the cBN seat is mounted on the upstream side of the DAC, however, the steel body of the DAC and highly absorbing metal gasket (preferably made of rhenium or tungsten) can efficiently attenuate majority of this signal.

2.3. Goniometers and data acquisition

At the APS and Advanced Light Source (ALS) high pressure beamlines, the goniometers available for single-crystal diffraction are simple one-axis (ω) or two-axis ($\omega + \chi$) devices with high motion precision and spheres of confusion smaller than 0.005 mm in diameter. The one-axis goniometers are equipped with a set of two motorized translation stages (\mathbf{xy}) that allow movement of the sample orthogonal to the rotation axis. An additional set of translation stages placed on the experimental table underneath the ω -rotation stage, allows aligning the rotation axis perpendicular to the beam, along \mathbf{y} , and translation of the sample along the rotation axis (\mathbf{z}). The two-axis goniometers are used mostly for combined SC μ XRD and Brillouin spectroscopy experiments, in which the Brillouin data is collected at different azimuthal angles. For the two-axis goniometers, the sample alignment with the χ -rotation axis is done manually. Since χ -scans are not used in the SC μ XRD data collection, the alignment of the sample with the χ -axis is not critical, and instead, multiple sample positions (translation stage motor settings) corresponding to the different discrete χ -settings can be defined for each of the sample crystals.

The SC μ XRD rotation images are collected using the ω -axis, which is normal to the incident beam, and defines the vertical direction of the instrument. There is no special procedure for assuring orthogonality of the ω -axis with the incident beam, therefore there is usually a small (less than 1°) angular misalignment, which does not affect the peak prediction by more than a single pixel.

Single-crystal experiments carried out in DACs suffer from very limited access to reciprocal space (see *e.g.* [27]). For experiments involving a four-circle diffractometer and point detector, Finger and King demonstrated that an optimal peak positioning mode, the fixed- ϕ mode, allows exploration of all accessible peaks.[34] With area detectors, the peak positioning is not individually controlled, but determined by the type of rotation scan performed and the crystal orientation, therefore no special consideration to the peak positioning mode is made. In order to achieve an optimal coverage of single-crystal data, as well as to maximize redundancy when using an Eulerian geometry goniometer (*e.g.* the simple 2-axis ω - χ setup), particularly in lower-symmetry crystal systems, it is always beneficial to perform ω -scans at several different χ angles. The increased redundancy factor facilitates identification of outliers resulting from extinction by strong diamond peaks, similar to the ψ -scan approach proposed for four-circle diffractometers by Loveday et al.[35]

2.4. Area detectors

Currently, GSE_ADA supports tiff and MAR image plate image formats. The program does not use any information stored in the headers of the diffraction image files. The information about the data collection conditions, rotation ranges and exposure times is supplied with the use of GSE_ADA GUI. The types of detectors that have been successfully used for SC μ XRD experiments with GSE_ADA/RSV data analysis thus far include MAR165 CCD, MAR345 IP and Perkin Elmer XRG1622.

In a typical area detector geometry used at the high pressure beamlines at the APS, the detector is placed centrally (incident beam hitting the detector surface close to the geometric center), normal to the incident beam. During alignment the angular offset of the detector from the normal position is minimized to be less than 1° using an iterative process of refining the detector geometry from

a powder pattern of a diffraction standard. Unlike in lab-diffractometers, high pressure beamline setups at APS at present do not have detector rotation stages (2θ). Instead, the detectors are mounted on two translation stages, allowing movement of the detector in the horizontal direction, normal to the beam (y), and change in the sample-to-detector distance (x). The positions of the detector stages are aligned only approximately with the setup reference coordinate system, therefore the use of diffraction images collected at multiple-detector positions requires a separate calibration for each detector position.

2.5. *Sample centering and working with multiple sample crystals*

For DAC experiments with a four-circle diffractometer, an efficient and accurate method for optimizing the sample alignment (centering) with the X-ray beam, based on eight-position centering of a group of diffraction peaks was introduced by King and Finger [36] and later generalized by Dera and Katrusiak.[37] For lab-based CCD diffractometers, an alternative approach based on analysis of radiographic images of the gasket hole at different DAC orientations was developed by Budzianowski and Katrusiak.[38] At the synchrotron beamlines, on the other hand, the availability of motorized sample translations makes it convenient to use the transmission-scan-based centering procedure (typically using the gasket hole absorption contrast) that was described in detail by Smith and Desgreniers.[39] The rotation axis is aligned with the X-ray beam by using a similar scanning technique in conjunction with a 0.010 mm diameter tungsten wire. As the sample is usually not exactly at the geometric center of the gasket hole, the final alignment with the X-ray beam is done using a high magnification online microscope. The point of reference for the microscope is determined by the observation of visible fluorescence induced by the incident beam illuminating a ruby chip pressure calibrant. The data collection position of each sample crystal is then defined with respect to this reference point.

In most single-crystal high pressure experiments carried out at the APS, multiple sample specimens are loaded into the same DAC. As the beam size is smaller than the samples (the beam is typically 0.003×0.005 mm and the samples have dimensions in the 0.005–0.030 mm range), separate data-sets are collected for each crystal. The use of multiple specimens brings several advantages: (1) if the quality of the specimens was not tested before DAC loading and one of the samples turns out to be of poor quality, there is a backup; (2) in case of observation of any discontinuous or otherwise interesting behavior (*e.g.* phase transition, color change, etc.), a second sample can be used to confirm that the observation was not an artifact (*e.g.* caused by bridging of the sample between the diamond anvils); and (3) multiple crystals with different orientations allow an option to merge the diffraction data, increasing both coverage as well as redundancy.

2.6. *Pressure transmitting media*

Single-crystal diffraction data are unquestionably more sensitive to the effects of nonhydrostatic stress than powder diffraction data. The presence of uniaxial stress distorts the crystal symmetry [40] as well as broadens and blurs the peaks, making two-dimensional peak-fitting less reliable. A number of recent high pressure studies have addressed the issue of the limits of true hydrostaticity and the extent of the uniaxial stress in different pressure media (*e.g.* [41,42]).

While single-crystal experiments with pressure media such as an alcohol mixture or argon are possible beyond 10 GPa (*e.g.* [1]), the quality of the information about the crystal structure is greatly reduced. Our general experience has been that only He and Ne (also H₂), result in high quality experiments beyond 12 GPa. At the APS, these gases can be conveniently loaded into DACs with the use of GSECARS/COMPRES gas-loading apparatus.[43] Both He and Ne preserve sharp diffraction peaks and good quality intensity data well beyond 50 GPa (*e.g.* [4,11,14]).

3. The data processing flow

3.1. Types of diffraction images

A typical SC μ XRD data-set for one single-crystal experiment consists of: (i) a set of calibration powder images for the different detector positions used (ii) a set of wide-rotation images (WRI) for different detector positions and χ settings (these images can also be obtained by merging the step images) and (iii) a set of step rotation images (SRI) covering the same rotation range as the WRIs. The WRIs at offset detector position are usually collected with two, or even four times longer exposures, since the majority of peaks contained in these images are weaker, due to the higher 2θ angles. It should be emphasized that the sample is rotated at constant speed during the collection of the SRIs. Typical SRIs analyzed with GSE_ADA have 1° angular increments. For samples with large unit cells the WRIs can have a significant spatial overlap of the peaks. Peak overlap can be minimized by splitting the available rotation range to several segments (*e.g.* 10° wide).

The detector-side angular access to the sample is typically restricted to less than $\pm 40^\circ$, and as a consequence, a variable portion of the detector active area remains shadowed by the diamond backing plate at all times. The shadowed regions of the detector do not contain any useful information, and in the WRI they unnecessarily lower the signal-to-noise statistics. To minimize this effect GSE_ADA can compute a dynamic mask (DM) that excludes the shadowed regions of the detector from analysis. The DM can be applied to each of the SRIs during merging to enhance signal to noise, in a way similar to the masking procedure described by Dawson et al.[44] A comparison of conventional WRI, and WRI obtained by merging a set of SRIs with the use of the DM is shown in Figure 3.

3.2. Detector calibration

In most high pressure experiments carried out at the APS, the energy of the incident beam is constrained by an absorption scan of a standard material, BaCO₃ (99.95% purity, CAS # 513-77-9) for example, and detection of the K absorption edge (the energy of the K-edge of Ba is 37.4406 keV [45]).

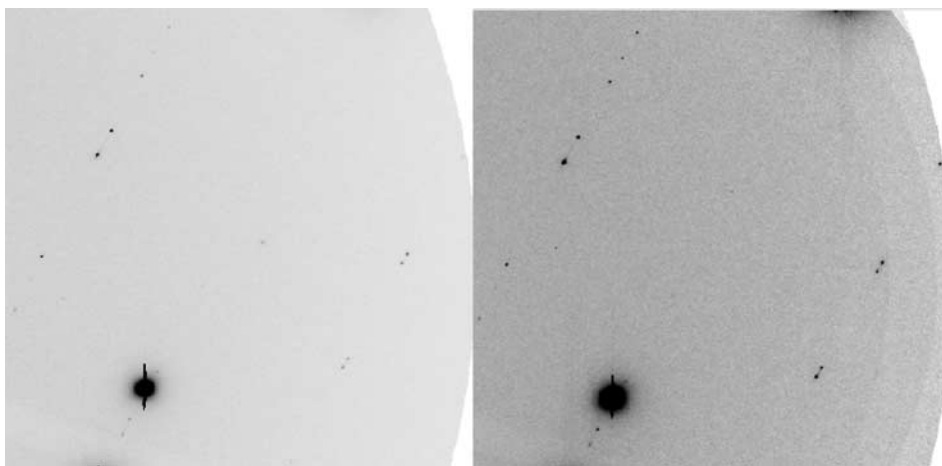


Figure 3. Comparison of simple WRI and result of merging SRIs covering the same rotation range with application of the DM.

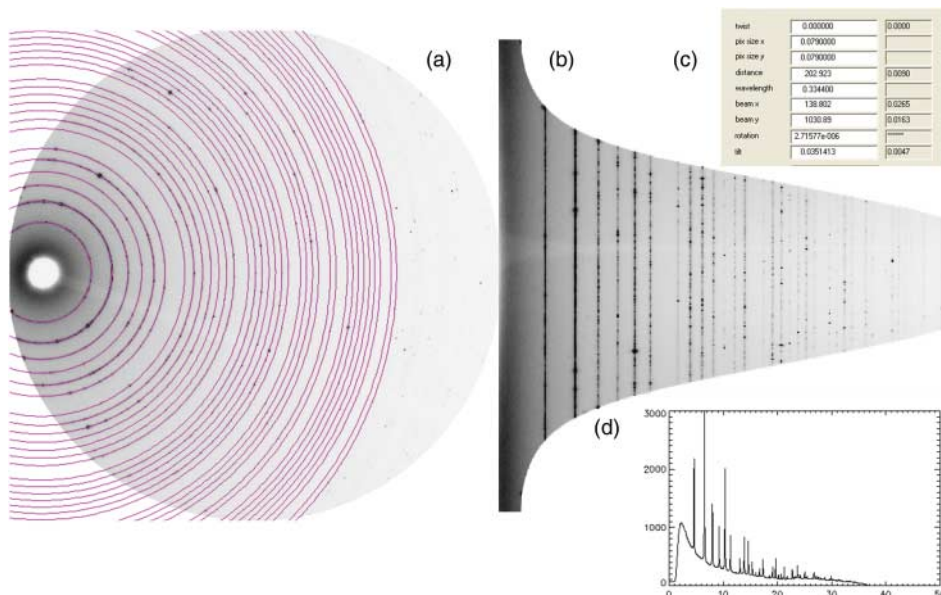


Figure 4. Detector geometry calibration in GSE_ADA for an offset detector position (transmitted beam intersecting the surface of the detector close to the detector edge): (a) calculated positions of the powder rings of calibration standard overlaid on the diffraction image, (b) cake transform, (c) refined calibration parameters with standard deviations, (d) integrated powder pattern of the diffraction standard.

The detector geometry (sample-to-detector distance, orientation of the vector normal in the laboratory reference system) is determined by using a powder diffraction image of a standard material, and can be done *e.g.* with the fit2d program.[46] GSE_ADA also allows automatic (w/o having to manually select any points in the diffraction image to define Debye–Scherrer rings) refinement of the detector calibration using conic detection algorithm. In GSE_ADA 1.6 there are two powder standards that are supported for the automated detector geometry calibration, CeO_2 (NIST standard 1979, $a = 5.4109(5) \text{ \AA}$ [47]) and LaB_6 (NIST standard 660, $a = 4.15646(5) \text{ \AA}$ [47]).

As illustrated in Figure 4, GSE_ADA calculates fit2d-style cake-transform [46] that can be used to assess the calibration reliability. It is also possible to perform a powder-style integration of the diffraction image, including masking capabilities (*e.g.* to remove diamond peaks from the image before integration) and overlay calculated Debye–Scherrer rings of the selected diffraction standard onto the diffraction image.

3.3. Peak search

After the diffraction images are collected and detector calibration is completed, the next step of data analysis is peak search. Unlike many other data analysis programs for area detectors, GSE_ADA typically performs the peak search on the WRI rather than on individual SRIs. GSE_ADA uses a search algorithm in which the intensity of each pixel in the image is compared with the local background. Peaks satisfying a threshold signal-to-noise ratio are selected for further analysis. In the initial search process some diamond peaks or points on powder rings (*e.g.* from the pressure transmitting medium) may be selected along with the sample peaks, but they are easy to identify and eliminate either by manual graphical selection, or automatically, after the orientation matrix is determined. After the peak search, a two-dimensional peak fit is performed to determine the pixel coordinates of each peak with maximum accuracy. Since the peak searches are conducted on WRIs, at this stage of the data analysis the rotation angles (RAs) at which each of the diffraction peaks has a maximum intensity are not yet known.

3.4. Analysis of the step scan to retrieve RAs

Once pixel coordinates of all peaks are determined, the SRIs are analyzed to retrieve each peak RA. During this analysis GSE_ADA determines the sum of pixel intensity (SPI) within a small region surrounding the center of each peak in the peak list in each of the images of the step-scan series. For good quality crystals the rocking curves of the peaks are much narrower than the 1° angular width of the SRI, and peaks are visible in only one or two consecutive SRIs. The center of the rotation range corresponding to the image in which the SPI is the highest is assigned to the given peak as the initial estimate of the RA.

Some area detectors, such as image plates, require an extended time to read the image after an exposure is completed. For example, the MAR345 image plate in full resolution mode (producing a 3450×3450 pixel image) takes over 2 min to read out, which is often longer than the actual exposure. This becomes particularly disadvantageous during a step scan, when many steps contribute to the idle time. GSE_ADA can also estimate the values of RA for most of the observed peaks without the step scan, using the dual slew method, in which an additional special WRI is recorded, where the sample rotation is accompanied by concurrent detector translation. The RAs are estimated from the displacement of the diffraction peaks in the standard and special WRI.[48] This method has been successfully used, for example in the study of Xe-H₂ compound at high pressure by Somayazulu et al.[13]

In GSE_ADA it is also possible to analyze step scans from variable-monochromatic single-crystal experiments, in which the incident energy, rather than the sample orientation, is gradually changed. The peak tables from such experiments can be analyzed and indexed in RSV in exactly the same way as standard monochromatic rotation-scan data.[17] Peak tables are passed between GSE_ADA and RSV through binary .pks files.

3.5. Peak indexing and orientation matrix determination

All steps of analysis that involve manipulation of vectors in reciprocal space, including peak indexing, orientation matrix determination and refinement, are conducted in RSV. RSV provides a graphical representation of the reciprocal vectors (lattice points) in a two-dimensional projection drawn along the x viewing direction. The direction of the projection can be manually changed. RSV provides an option for simple manipulation of the set of vectors in the peak table, including select/de-select and filtering (*e.g.* using a maximum intensity threshold).

RSV offers a built-in indexing algorithm that utilizes a difference vector frequency analysis approach. Alternatively, a plugin to the CELL_NOW program [29] is provided. Upon successful peak indexing, an orientation matrix (UB matrix) is determined, following the convention described by Busing and Levy.[30] RSV features the ability to filter the set of peaks and select ones that do not conform to the current orientation matrix (*i.e.* their calculated Miller indices depart from integer numbers by more than a given threshold value). The program offers two separate memory bins to separate the reciprocal vectors into subsets; especially useful in cases of sample twinning or working with multiple sample crystals with overlapping signals.

Once peaks are successfully indexed, a plugin to the XPREP program [28] is used to search for transformations to higher symmetry settings and determination of space group symmetry.

3.6. Refinement of the unit cell and identification of outliers

After the standard unit cell setting is chosen, a refinement of the orientation matrix and unit cell parameters is performed, applying symmetry constraints. RSV uses a refinement approach in which only d -spacings of the vectors are taken into account, instead of full Cartesian coordinates

of each reciprocal vector, utilizing the Levenberg–Marquardt minimization procedure [49] implemented in the MPFIT library, with numerical evaluation of partial derivatives of each optimized parameter. The reason for d -spacing-based refinement is that the typical angular steps used in data collection (1°) introduce a fairly large uncertainty into the orientation of the reciprocal vectors, while their lengths are very well constrained by the pixel coordinates. The uncertainties reported by RSV are 1 sigma errors computed from the covariance matrix. RSV offers graphical identification of pseudosymmetry, so as to avoid assigning improper high symmetry. After the refinement of the orientation matrix and unit cell parameter the program displays a plot in which normalized error in d -spacing for each of the peaks,

$$\frac{d_{\text{obs}}^i - d_{\text{calc}}^i}{d_{\text{calc}}^i}, \quad (1)$$

where d_{obs}^i is the observed d -spacing and d_{calc}^i is the same d -spacing calculated from the refined unit cell parameters, is displayed as a function of the RA. If the selected symmetry constraints are incorrect, a clear functional dependence of (1) can be seen. The d -spacing error plot can also identify outliers, incorrectly indexed peaks, or peaks that do not belong to the sample, but happen to be close to the predicted peak position for a sample peak.

An example of the d -spacing error analysis with RSV is presented in Figure 5. The sample crystal in this case was a triclinic phase with P1 symmetry and pseudo-monoclinic unit cell. With triclinic constraints, a proper scatter of peaks around $y = 0$ indicates correct symmetry, yielding refined unit cell parameters $a = 15.505(3)\text{ \AA}$, $b = 9.580(6)\text{ \AA}$, $c = 9.044(1)\text{ \AA}$, $\alpha = 90.12(3)$, $\beta = 93.83(2)$, $\gamma = 90.89(3)$. With the improper monoclinic constraints, the refined unit cell seems reasonable: $a = 15.465(3)\text{ \AA}$, $b = 9.452(6)\text{ \AA}$, $c = 9.048(2)\text{ \AA}$, $\beta = 93.94(2)$, but a grouping of peaks into a functional dependence indicates incorrect symmetry.

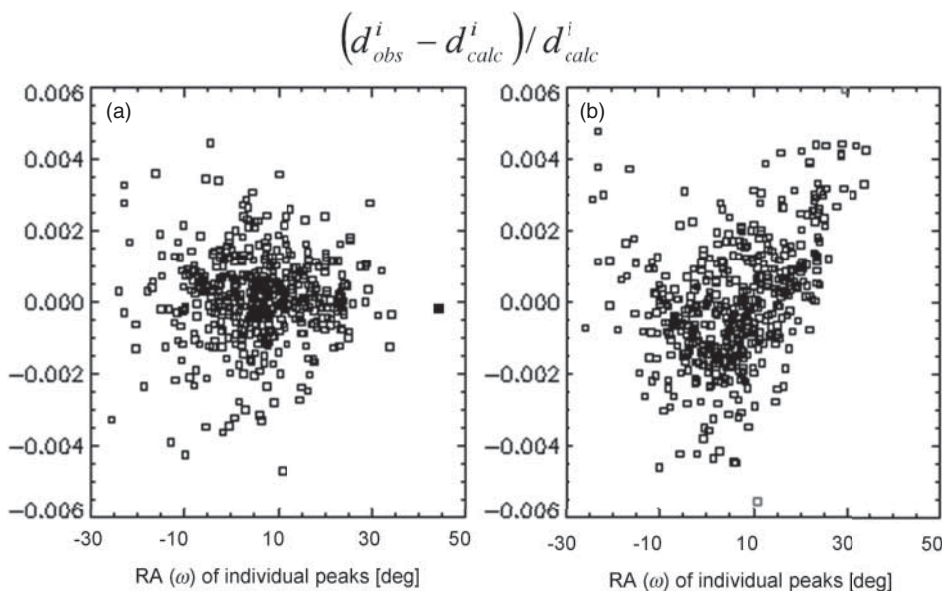


Figure 5. An example of the d -spacing error analysis with RSV for a triclinic crystal with P1 symmetry and pseudo-monoclinic unit cell: (a) with triclinic constraints proper scatter of peaks around $y = 0$ indicates correct symmetry, (b) with monoclinic constraints a grouping of peaks into a functional dependence indicates incorrect symmetry. The triclinic symmetry assignment is confirmed by peak intensities.

Once the orientation matrix is determined, RAs can be refined for each peak. This refinement is usually not necessary, however, as the final peak list is generated during peak prediction, in which case accurate RAs are calculated.

3.7. Peak prediction

Once the orientation matrix of the crystal is determined, this information is stored in an ASCII file (.ub). This file can then be imported to GSE_ADA and used to simulate the pixel coordinates and RAs of all peaks that should be observable within the given rotation range and opening of the DAC. By predicting peak positions it is usually possible to locate more peaks than found during the peak search because for peaks with lower intensities that did not satisfy the signal to noise requirement of the peak search, it may still be possible to successfully carry out profile refinement. In the current version, GSE_ADA only uses peak intensities determined by the fitting algorithm, and simple pixel summation is not supported.

GSE_ADA defines a Bravais lattice type (determined from the initial list of peaks obtained in the peak search using XPREP by analyzing the systematic absences), and uses the extinction rules for the selected Bravais type when predicting peaks.

When all predicted peak positions within the given rotation range are calculated, GSE_ADA provides a filtering capability to identify which of the peaks are observed. Typically, the predicted but unobserved peaks are selected and removed from the data-set prior to final peak fitting and the GSE_ADA output does not contain unobserved peaks. Peaks from different detector positions and different χ -settings are processed separately and merged/scaled after the peak fitting is completed. The merge scaling factors for the different peak tables can be conveniently determined in XPREP.

In addition to the simulation of monochromatic diffraction, GSE_ADA can also calculate peak positions for polychromatic Laue diffraction in a given energy range, using the same orientation matrix.

3.8. Peak fitting and peak intensity corrections

GSE_ADA uses two-dimensional peak fitting with either seven-parameter Gaussian or eight-parameter pseudo-Voigt function with a flat background to constrain pixel coordinates and integrated intensities of each of the observed diffraction peaks. The two-dimensional Gaussian profile is defined as follows:

$$G(x, y) = B + S e^{-1/2(((x-x_0) \cos \varphi - (y-y_0) \sin \varphi)/a_x)^2 + ((x-x_0) \sin \varphi + (y-y_0) \cos \varphi)/a_y)^2}, \quad (2)$$

where x_0 and y_0 are pixel coordinates of the peak center, a_x and a_y are elliptical axial lengths (peak widths) in unrotated coordinates, φ is the rotation angles of the Gaussian ellipse with respect to the detector reference frame, B is the flat background term and S is the intensity scale factor. GSE_ADA does not use model profiles (*i.e.* a function that ties together profile parameters of different peaks) and does not support $K\alpha_1 + K\alpha_2$ fitting.

If a peak is selected in the peak table, the results of the peak fitting are displayed in the graphical windows of the 'Peaks' tab, shown in Figure 1. The top-left image is the zoom of the actual measured diffraction pattern, the top-right image is the corresponding fit profile, and the bottom image shows the difference between the observed and calculated profiles. The program allows the user to define the pixel size of the fitting window to either be the same for all the peaks, or be individually adjusted for each peak, in case if there is a significant anisotropy of peak profiles, or when some peaks are closely spaced.

In order to allow structure determination, a set of corrections is applied to the measured peak intensities $I(hkl)$ to calculate structure factors $|F(hkl)_{\text{obs}}|^2$. The corrections available in GSE_ADA include Lorenz and polarization factors, absorption correction for cBN backing plates and empirical sample displacement/shape correction.

3.8.1. Symmetric consistency-based correction

The first point of data analysis where intensity corrections are applied is at the completion of peak fitting with RA already determined. At this stage the symmetry of the crystal has also been determined with the use of XPREP, and it is possible to use the information about the symmetry-dependence of peaks within the given crystal system to look for systematic errors. In the majority of the DAC SC μ XRD experiments, the X-ray beam is smaller or comparable in size to the sample, and changes in the sample illuminated volume at this size scale (1–10 μm) are unavoidable. While ideally a monochromatic beam should be much larger than the sample, the feasibility and reliability of crystal structure determination with beam smaller than the sample has been investigated in detail [50,51] with a conclusion confirming that, with carefully applied corrections, the quality of the data is not significantly affected.

GSE_ADA offers an empirical correction to identify systematic errors, which are rotation-angle dependent (*e.g.* sample moving in the beam during rotation). Figure 6 illustrates this process with real example of diffraction data on orthorhombic ferrosilite (FeSiO_3) crystal collected in the DAC.[3] The x -axis shows the RA of each peak and the quantity plotted is

$$\frac{I_{\text{obs}}^i - \langle I_{\text{obs}}^{\text{symm}} \rangle}{\langle I_{\text{obs}}^{\text{symm}} \rangle}, \quad (3)$$

where I_{obs}^i is an individual measured peak intensity, and $\langle I_{\text{obs}}^{\text{symm}} \rangle$ is an average intensity in the group of symmetry-dependent peaks to which i belongs.

A majority of the peaks cluster around $y = 0$ and show a slight functional dependence on RA, which can be modeled by a polynomial. A few outlier peaks are also seen that significantly

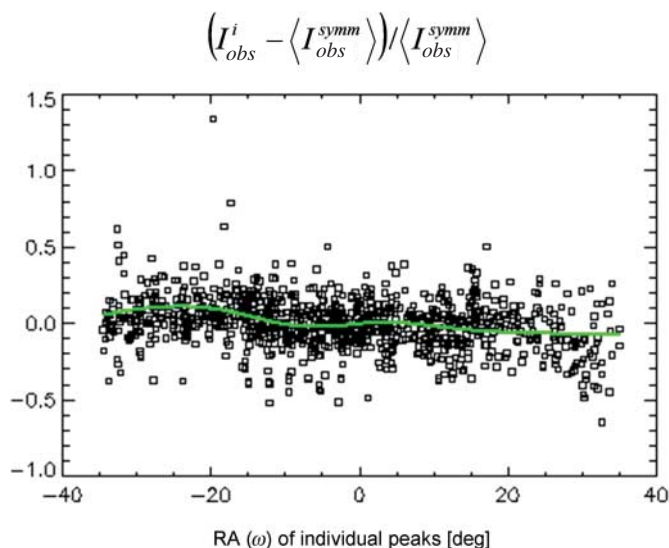


Figure 6. An example of the symmetric consistency correction in GSE_ADA for the jadeite crystal data at 8.2(1) GPa described in Section 4. A slight functional trend (green line represents polynomial fit) indicates movement of the sample in the beam during rotation.

disagree with their symmetry equivalents. The importance of outlier rejection in processing DAC single-crystal data has recently been emphasized by Friese et al.[52] In the data correction process with GSE_ADA the outliers are identified and removed and the polynomial correction is applied. Since the rotation-angle dependent errors are likely to be the same for data collected at different detector positions, it is recommended to merge the corresponding peak tables prior to applying this correction.

3.8.2. *Diamond absorption*

During a single-crystal DAC experiment, for each of the diffraction peaks both the incident and diffracted beams travel through the diamond anvils and experience absorption. The absorption coefficient of diamond at the typical incident energy $E = 30$ keV is 0.058 mm^{-1} , which corresponds to 11% absorption through the 2 mm thickness of each of the diamonds. For a typical DAC with an opening angle of $+30^\circ$, the length of the path of the X-ray beams through the diamond can vary up to 15%, which brings the variation in the absorption effect from peak to peak to less than 2%. In GSE_ADA the diamond absorption effect by the downstream anvil is ignored, whereas the effect of the upstream anvil can be accounted for through one of the omega-dependent corrections described below.

GSE_ADA offers an option to output the peak list in ASCII format, including information about the diffracted beam direction vectors that can be used to apply any custom corrections using other software.

3.8.3. *Backing plate absorption*

The absorption correction procedure for DACs equipped with symmetric beryllium backing plates has been discussed by Angel.[53] As explained in Section 2.2, a cBN backing plate on the incident beam side is a common and convenient option used in the SC μ XRD experiments. The cBN backing plate, while semi-transparent to the X-rays, absorbs the incident beam to a significant degree and requires an absorption correction. With the cBN backing plate placed on the incident beam side and ω -rotation the correction is only dependent on the RA and can be simply and reliably measured using the DAC with the sample loaded, and a photodiode detector placed behind the DAC, on the transmitted beam path. An example of such absorption profile is shown in Figure 7. The central part of the profile, with the highest transmission, corresponds to the conical access hole in the cBN plate. The cutoff angles seen in Figure 7 are determined by the opening angle of the BA backing plate on the detector side. The incident beam still illuminates the sample at $\omega > 25^\circ$ and $\omega < -25^\circ$, until the body of the DAC cuts it off, which in the example shown in Figure 7 takes place at $\omega > 30^\circ$ and $\omega < -30^\circ$, however, the transmitted beam measured by the photodiode is attenuated by the detector-side seat beyond $\omega = \pm 25^\circ$. GSE_ADA allows to calculate the angle-dependent absorption effect of the cBN seat from the seat geometry, using parameters that can either be physically measured or empirically adjusted to obtain the best match of the calculated and measured profile.

3.8.4. *Lorenz and polarization effects*

Lorenz and polarization factors (L_p) are well-known corrections used in single-crystal XRD analysis. The DAC does not modify the way in which these corrections are applied. GSE_ADA uses an L_p correction model described by He.[54]

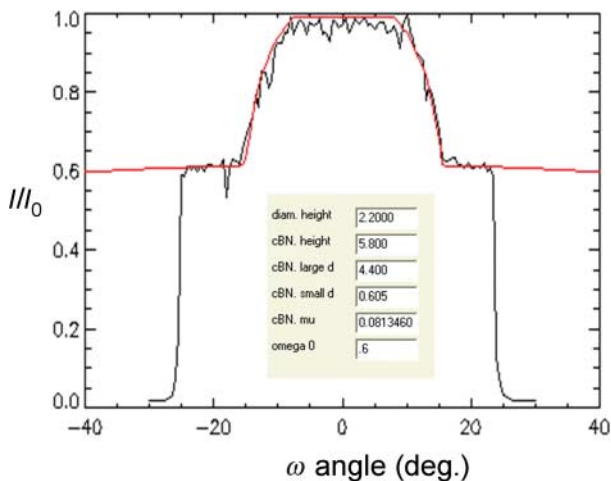


Figure 7. Absorption profile of the cBN backing plate mounted on the upstream side of the DAC measured with a photodiode detector (black line) vs. analytical absorption correction in GSE_ADA (red line). Shown in the inset are the parameters used to calculate the correction.

3.8.5. Model-biased correction

The final correction offered by GSE_ADA is based on the comparison of peak intensities calculated from a starting crystal structure model with observed intensities. Merging of symmetry-dependent intensity data must be disabled (*e.g.* MERG 0 instruction in SHELXL) for this correction. Similar to the symmetric consistency correction, for the model-biased correction GSE_ADA plots the intensity error, this time defined as

$$\frac{I_{\text{obs}}^i - I_{\text{calc}}^i}{I_{\text{calc}}^i}, \quad (4)$$

where I_{calc}^i is the peak intensity calculated from the structure model, as a function of selected experimental variable (RA, 2θ angle or azimuth angle) and looks for outliers and functional dependencies that can be modeled with a use of a simple polynomial. The use of $I_{\text{obs}}/I_{\text{calc}}$ analysis in identifying outliers has also been advocated by Friese et al.[52] Such analysis is often more advantageous for identifying subtle systematic error effects and outliers than the symmetric consistency correction described in Section 3.8.1, particularly for data-sets with low redundancy. However, caution has to be exercised when using a model-biased correction to avoid overcorrecting the data and ‘forcing’ an incorrect model.

4. Reliability of structure analysis with GSE_ADA/RSV

The GSE_ADA/RSV software is optimized to handle data collected at very high pressure, however, it is also easily applied to samples in air and at lower pressure. We conducted a number of tests and comparisons in which synchrotron single-crystal data were collected using the procedures described above and then analyzed with GSE_ADA/RSV, leading to structure refinements with SHELX. In each case an excellent agreement with previously published crystal structures was found.

An example of a high pressure SC μ XRD structure determination for NaAl(SiO₃)₂ clinopyroxene jadeite at 8.2(1) GPa is described in Tables 1–3, compared with earlier lab results on the same sample at 7.83(5) GPa.[55] The synchrotron data were collected at the experimental station

Table 1. Crystal data and structure refinement for jadeite at 8.2(1) GPa in Ne pressure medium compared with lab-diffractometer data on the same sample (different, larger crystal) at 7.83(5) GPa in alcohol medium.[55]

Empirical formula	NaAl (Si ₂ O ₃) ₂	
Temperature	293(2) K	293(2) K
Pressure	8.2(1) GPa	7.83(5) GPa
Wavelength	0.3344 Å	0.7107 Å
Crystal system, space group	monoclinic, C2/c	
Unit cell dimensions	$a = 9.243(3) \text{ \AA}$	$9.2455(4) \text{ \AA}$
	$b = 8.407(3) \text{ \AA}$	$8.4137(8) \text{ \AA}$
	$c = 5.1220(5) \text{ \AA}$	$5.1269(4) \text{ \AA}$
	$\beta = 106.847(11)^\circ$	$106.710(4)^\circ$
Volume	$V = 380.9(2) \text{ \AA}^3$	$381.57(5) \text{ \AA}^3$
Reflections collected/unique	468/212	283/236
	($R_{\text{int}} = 0.087$)	
R-indices (all data)	$R_1 = 0.0470$	$R_1 = 0.0450$

Table 2. Fractional atomic coordinates and equivalent isotropic displacement parameters ($\text{\AA}^2 \times 10^3$) for the jadeite structure determination.

Atom	x	y	z	U(eq)
Synchrotron, at $p = 8.2$ (1) GPa				
Na (1)	0	0.3052 (5)	0.2500	11 (1)
Al (1)	0	0.0920 (3)	0.7500	7 (1)
Si (1)	0.2907 (2)	0.0953 (2)	0.2293 (2)	7 (1)
O (1)	0.1097 (5)	0.0789 (5)	0.1307 (6)	7 (1)
O (2)	0.3587 (5)	0.2679 (6)	0.3018 (6)	9 (1)
O (3)	0.1423 (5)	0.4861 (6)	-0.0013 (5)	8 (1)
Lab, at $p = 7.83$ (5) GPa [55]				
Na (1)	0	0.3025 (6)	0.2500	14.3 (8)
Al (1)	0	0.0919 (4)	0.7500	7.8 (5)
Si (1)	0.2913 (2)	0.0948 (2)	0.2291 (3)	8.2 (4)
O (1)	0.1085 (3)	0.0789 (6)	0.1293 (7)	7.5 (8)
O (2)	0.3602 (4)	0.2672 (7)	0.3024 (6)	10.9 (9)
O (3)	0.3570 (4)	0.4852 (7)	-0.0016 (6)	9.2 (8)

Note: $U(\text{eq})$ is defined as one-third of the trace of the orthogonalized U_{ij} tensor.

Table 3. Selected bond lengths for jadeite [\AA].

	Synchrotron 8.2 (1) GPa	Lab [55] 7.83 (5) GPa
Na(1)-O(1)#1	2.320 (5)	2.310 (6)
Na(1)-O(2)#4	2.370 (4)	2.360 (4)
Na(1)-O(3)#2	2.337 (5)	2.354 (6)
Na(1)-O(3)	2.585 (5)	2.595 (5)
Al(1)-O(1)#1	1.922 (3)	1.915 (3)
Al(1)-O(1)#10	1.956 (4)	1.957 (4)
Al(1)-O(2)#5	1.835 (5)	1.827 (5)
Si(1)-O(1)	1.607 (5)	1.623 (3)
Si(1)-O(2)	1.582 (5)	1.585 (5)
Si(1)-O(3)#13	1.623 (3)	1.611 (4)
Si(1)-O(3)#14	1.634 (4)	1.636 (5)

Notes: Symmetry transformations used to generate equivalent atoms:

#1 $-x, y, -z + 1/2$, #2 $x, -y + 1, z + 1/2$, #3 $-x, -y + 1, -z$, #4 $x - 1/2, -y + 1/2, z - 1/2$, #5 $-x + 1/2, -y + 1/2, -z + 1$, #6 $-x + 1/2, y + 1/2, -z + 1/2$, #7 $x - 1/2, y + 1/2, z$, #8 $x - 1/2, -y + 1/2, z + 1/2$, #9 $x, y, z + 1$, #10 $-x, -y, -z + 1$, #11 $x, -y, z + 1/2$, #12 $-x, -y, -z + 2$, #13 $-x + 1/2, -y + 1/2, -z$, #14 $-x + 1/2, y - 1/2, -z + 1/2$, #15 $x + 1/2, y - 1/2, z$, #16 $x, y, z - 1$

13IDD with a 0.003×0.003 mm focused beam at incident energy of 37.07 keV, using a symmetric Princeton DAC with a combination of cBN and BA seats, and an opening angle of $\pm 25^\circ$. Only one sample crystal and one χ -setting were measured (as described above, the quality of the refinement could be significantly improved by using more than one sample crystal and multiple χ -settings). Diffraction images were collected with a MAR165 CCD detector placed at ~ 200 mm from the sample, at three positions differing by a translation along y by 70 mm. The total data collection time was about 5 min. For comparison, the data collection on the lab instrument took about 24 h.[55]

Comparison of the structure refinement results in Tables 1–3 shows that the SC μ XRD is typically characterized by lower symmetric consistency of peak intensities (higher R_{int}) than the highest quality lab-based four-circle diffractometer measurements, but the higher redundancy of the SC μ XRD data compensates for this effect and still allows for very reliable structure refinements (see the agreement of fractional atomic coordinates in Table 2 and the comparable standard deviations). Also the precision of the unit cell parameter determination using the eight-position centering method is usually superior to SC μ XRD, however we find the equation of state results to be very consistent with earlier lab-based measurements. Comparisons of other high pressure data in a lower pressure regime, where previous investigations utilizing four-circle lab diffractometer are available, yield similarly reassuring agreements.[5,15] Figure 8 shows an example of the pressure evolution of fractional atomic coordinates of SiO₂ α -cristobalite determined from a synchrotron experiment with GSE_ADA data analysis [5] and on a lab diffractometer.[56] In case of one sample (Cr₂O₃, measured to 55 GPa [4,57]), we were also able to evaluate the

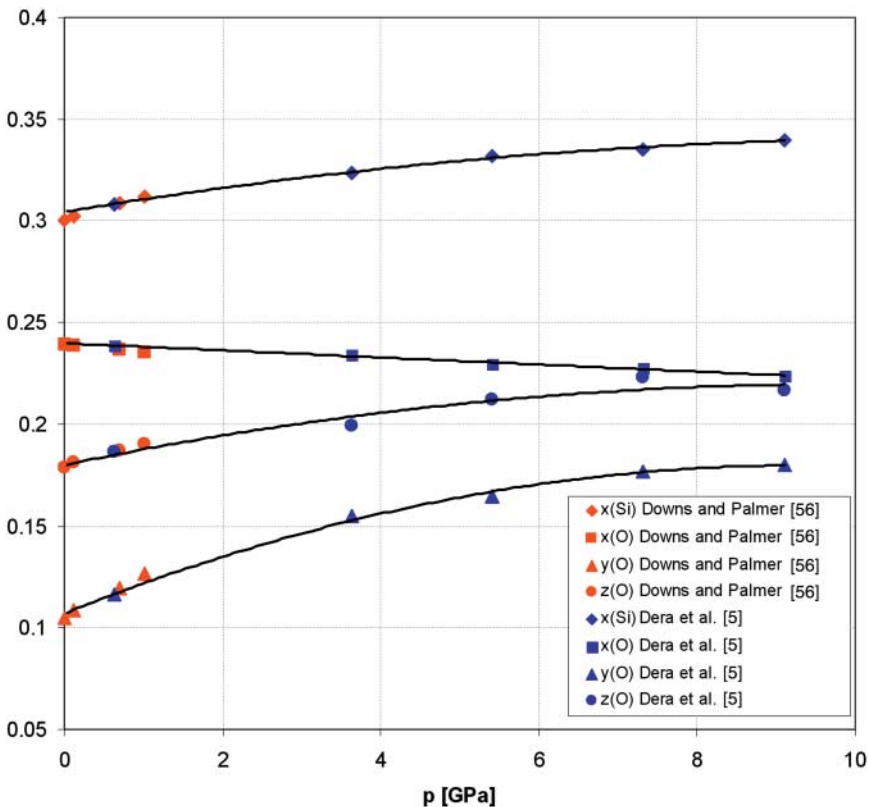


Figure 8. Consistency of trends in the pressure-dependence of SiO₂ α -cristobalite fractional atomic coordinates determined in synchrotron SC μ XRD experiment [5] and in a lab experiment on a four-circle diffractometer.[56]

consistency of SC μ XRD data from independent synchrotron experiments conducted by different research groups on the same sample compound, and processed with different data analysis software packages (GSE_ADA/RSV vs. Agilent CrysAlis) and also found an excellent agreement.

5. Conclusions

GSE_ADA/RSV is reliable, versatile and free software for processing synchrotron SC μ XRD data to obtain accurate unit cell parameters and integrated peak intensity information. This information can be used for equation of state studies, refinement of known structures, and determination of unknown structure of crystalline phases. The software is well suited for analyzing single-crystal diffraction data collected from samples loaded in DACs and includes a variety of corrections and tools that address the specific conditions and constraints of diffraction experiments with DACs.

Acknowledgements

The development of this software was initially funded through NSF DMR Major Research Instrumentation project 0521179 to UNLV. We acknowledge the support and encouragement by M.F. Nicol. O.G.-U. and O.T. acknowledge support through the NNSA Cooperative Agreement DE-FC88-01NV14049.

GeoSoilEnviroCARS is supported by the National Science Foundation – Earth Sciences (EAR-0622171) and the Department of Energy – Geosciences (DE-FG02-94ER14466). The APS is supported by DOE-BES, under Contract No. DE-AC02-06CH11357. The ALS is supported by the Director, Office of Science, Office of Basic Energy Sciences, of the U.S. Department of Energy under Contract No. DE-AC02-05CH11231.

Notes

1. <http://www.exelisvis.com/ProductsServices/IDL.aspx>.
2. <http://cow.physics.wisc.edu/~craigm/idl/idl.html>.
3. <http://www.idlcoyote.com/index.html>.
4. http://cars9.uchicago.edu/software/idl/detector_routines.html.

References

- [1] Dera P, Lavina B, Borkowski LA, Prakapenka VB, Sutton S, Rivers ML, Downs RT, Bector NZ, Prewitt CT. High-pressure polymorphism of Fe₂P and its implications for meteorites and earth's core. *Geophys Res Lett*. 2008;36:L10301 (6pp.).
- [2] Chen B, Gao L, Lavina B, Dera P, Alp E, Zhao J, Li J. Magneto-elastic coupling in compressed Fe₇C₃ supports carbon in Earth's inner core. *Geophys Res Lett*. 2012;39:L18301 (4pp.).
- [3] Dera P, Finkelstein G, Duffy TS, Downs RT, Meng Y, Prakapenka V, Tkachev S. Metastable high-pressure transformations of orthoferrosilite Fe₈S₂. *Phys Earth Planet Inter*. 2013, in press.
- [4] Dera P, Lavina B, Meng Y, Prakapenka VB. Structural and electronic evolution of Cr₂O₃ on compression to 55 GPa. *J Solid State Chem*. 2011;184:3040–3049.
- [5] Dera P, Lazarz J, Prakapenka VB, Barkley M, Downs RT. New insights into high-pressure polymorphism of SiO₂ cristobalite. *Phys Chem Miner*. 2011;38:517–529.
- [6] Dera P, Lazarz JD, Lavina B. Pressure-induced development of bonding in NiAs type compounds and polymorphism of NiP. *J Solid State Chem*. 2011;184:1997–2003.
- [7] Dera P, Nisar J, Ahuja R, Tkachev S, Prakapenka VB. New type of possible high-pressure polymorphism in NiAs-type minerals in planetary cores. *Phys Chem Miner*. 2013;40:183–193.
- [8] Finkelstein G, Dera P, Jahn S, Oganov A, Holl C, Meng Y, Duffy T. Phase transitions and equation of state of forsterite to 90 GPa from single-crystal X-ray diffraction and molecular modeling. *Am Mineral*, in press.
- [9] Lavina B, Dera P, Downs RT, Prakapenka V, Rivers ML, Sutton S, Nicol MF. Siderite at lower mantle conditions, the effects of the pressure-induced spin-pairing transition. *Geophys Res Lett*. 2009; 36: L23306 (4pp.).
- [10] Lavina B, Dera P, Downs RT, Tschauer O, Yang W, Shebanova O, Shen G. Effect of Fe dilution on the spin pairing transition in rhombohedral carbonates. *High Press Res*. 2010;30:224–229.
- [11] Lavina B, Dera P, Downs RT, Yang W, Sinogeykin S, Meng Y, Shen G, Schiferl D. Structure of siderite FeCO₃ to 56 GPa and hysteresis of its spin-pairing transition. *Phys Rev B*. 2010;82:064110 (7pp.).

- [12] Lavina B, Dera P, Kim E, Meng Y, Downs RT, Weck PF, Sutton SR, Zhao Y. Fe₄O₅, a new, recoverable, high pressure-temperature iron oxide. *Proc Natl Acad Sci USA*. 2011;108:17281–17285.
- [13] Somayazulu M, Dera P, Goncharov AF, Gramsch SA, Liu Z, Mao HK, Hemley RJ, Liermann P. Pressure-induced bonding and compound formation in xenon-hydrogen solids. *Nature Chem*. 2009;2: 50–53.
- [14] Plonka A, Dera P, Irmen P, Rivers ML, Ehm L, Parise JB. β -diopside, a new ultrahigh-pressure polymorph of CaMgSi₂O₆ with six-coordinated silicon. *Geophys Res Lett*. 2012;39:L24307 (4pp.).
- [15] Thompson RM, Downs RT, Dera P. The compression pathway of quartz. *Am Mineral*. 2011; 96:1495–1502.
- [16] Tschauner O, Grubor-Urošević O, Dera P, Mulcahy S. Anomalous elastic behaviour in Hcp- and Sm-type dysprosium. *J Phys Chem C*. 2012;116: 2090–2096.
- [17] Wang Y, Hilairet N, Dera P. Recent advances in high pressure and temperature rheological studies. *J Earth Sci*. 2010;21:495–516.
- [18] Ye Y, Brown DA, Smyth JR, Panero WR, Jacobsen SD, Chang Y-Y, Townsend JP, Thomas S-M, Hauri EH, Dera P, Frost DJ. Compressibility and thermal expansion of hydrous ringwoodite with 2.5(3) wt% H₂O. *Am Mineral*. 2012;97:573–582.
- [19] Ye Y, Smyth JR, Hushur A, Lonappan D, Manghnani M, Dera P, Frost D. Crystal structure and hydration mechanism in hydrous wadsleyite with 2.8 percent H₂O and compressibility to 60 GPa. *Am. Mineral*. 2010;95:1765–1772.
- [20] Ye Y, Smyth JR, Jacobsen SD, Panero WR, Brown DA, Katsura T, Chang YY, Townsend JP, Dera P, Tkachev S, Untenborn C, Liu Z, Goujon C. Crystal structure, Raman and FTIR spectroscopy and equations of state of OH-bearing MgSiO₃ akimotoite. *Contrib. Mineral. Petrol.*, in press.
- [21] Zhang J, Dera P, Bass JD. A new high-pressure phase transition in iron-bearing orthoenstatite: an anisotropy discontinuity in the upper mantle? *Am Mineral*. 2012;97:1070–1074.
- [22] Zhang L, Meng Y, Dera P, Yang W, Mao WL, Mao H-K. Single-crystal structure determination of (Mg,Fe)SiO₃ postperovskite. *Proc Natl Acad Sci USA*. 2013;110:6292–6295.
- [23] Zhuravlev KK, Goncharov AF, Tkachev SN, Dera P, Prakapenka VB. Vibrational, elastic, and structural properties of cubic silicon carbide under pressure up to 75 GPa: implication for a primary pressure scale. *J Appl Phys*. 2013;113:113503 (12pp.).
- [24] Guionneau P, Pevelen DL, Marchivie M, Pechev S, Gaultie J, Barrans Y, Chasseau D. Laboratory high-pressure single-crystal X-ray diffraction – recent improvements and examples of studies. *J Phys Condens Matter*. 2004;16:S1151–S1159.
- [25] Hazen RM, Finger LW. Comparative crystal chemistry: temperature, pressure, composition and the variation of crystal structure. Chichester: John Wiley & Sons; 1982.
- [26] McMahon MI. High-pressure crystallography. *Top Curr Chem*. 2012;315:69–110.
- [27] Miletich R, Allan DR, Kuhs WF. High-pressure single-crystal techniques. In: Hazen RM, Downs RT, editors. High-temperature and high pressure crystal chemistry. Washington (DC): Mineralogical Society of America; 1999. p. 445–520.
- [28] Sheldrick GM. XPREP ver. 5.1. Madison: Bruker AXS; 1997.
- [29] Sheldrick GM. CELL_NOW. Göttingen: University of Göttingen; 2008.
- [30] Busing WR, Levy HA. Angle calculations for 3- and 4- circle X-ray and neutron diffractometers. *Acta Cryst*. 1967;22:457–464.
- [31] Casati N, Macchi P, Sironi A. Improving the quality of diamond anvil cell data collected on an area detector by shading individual diamond overlaps. *J Appl Cryst*. 2007;40:628–630.
- [32] Periotto B, Nestola F, Balic-Zunic T, Angel RJ, Miletich R, Olsen LA. Comparison between beryllium and diamond-backing plates in diamond anvil cells: application to single-crystal x-ray diffraction high-pressure data. *Rev Sci Instrum*. 2011;82:055111 (5pp.).
- [33] Boehler R, Hantsetters Kd. New anvil designs in diamond-cells. *High Press Res*. 2004;24:391–396.
- [34] Finger LW, King H. A revised method of operation of the single-crystal diamond cell and refinement of the structure of NaCl at 32 kbar. *Am Mineral*. 1978;63:337–342.
- [35] Loveday JS, McMahon MI, Nelmes RJ. The effect of diffraction by the diamonds of a diamond-anvil cell on single-crystal sample intensities. *J Appl Cryst*. 1990;23:392–396.
- [36] King H, Finger LW. Diffracted beam crystal centering and its application to high-pressure crystallography. *J Appl Crystallogr*. 1979;12:374–378.
- [37] Dera P, Katrusiak A. Diffractometric crystal centering. *J Appl Crystallogr*. 1999;32:510–515.
- [38] Budzianowski A, Katrusiak A. High-pressure crystallographic experiments with a CCD-detector. In: Katrusiak A, McMillan PF, editors. High-pressure crystallography. Dordrecht: Kluwer; 2004. p. 101–112.
- [39] Smith JS, Desgreniers S. Selected techniques in diamond anvil cell crystallography: centering samples using X-ray transmission and rocking powder samples to improve X-ray diffraction image quality. *J Synchrotr Rad*. 2008;16:83–96.
- [40] Downs RT, Singh AK. Analysis of deviatoric stress from nonhydrostatic pressure on a single crystal in a diamond anvil cell: the case of monoclinic aegirine, NaFeSi₂O₆. *J Phys Chem Solids*. 2006; 67: 1995–2000.
- [41] Angel RJ, Bujak M, Zhao J, Gatta GD, Jacobsen SD. Effective hydrostatic limits of pressure media for high-pressure crystallographic studies. *J Appl Crystallogr*. 2007;40:26–32.
- [42] Klotz S, Chervin J-C, Munsch P, Marchand GL. Hydrostatic limits of 11 pressure transmitting media. *J Phys D Appl Phys*. 2009;42:075413 (7pp).
- [43] Rivers M, Prakapenka VB, Kubo A, Pullins C, Holl CM, Jacobsen SD. The COMPRES/GSECARS gas-loading system for diamond anvil cells at the Advanced Photon Source. *High Press Res*. 2008;28: 273–292.

- [44] Dawson A, Allan DR, Parsons S, Ruf M. Use of a CCD diffractometer in crystal structure determinations at high pressure. *J Appl Cryst.* 2004;37:410–416.
- [45] Bearden JA, Burr AF. Reevaluation of X-ray atomic energy levels. *Rev Mod Phys.* 1967;39:125–142.
- [46] Hammersley AP, Svensson SO, Hanfland M, Fitch AN, Häusermann D. Two-dimensional detector software: from real detector to idealised image or two-theta scan. *High Press Res.* 1996; 14:235–248.
- [47] O'Connor BH, Pratapa S. Improving the accuracy of Rietveld-derived lattice parameters by an order of magnitude. *Adv X-Ray Anal.* 2002;45:158–165.
- [48] Dera P. All different flavors of synchrotron single crystal X-ray diffraction experiment. In: Boldyreva E, Dera P, editors. *High-pressure crystallography: from fundamental phenomena to technological applications.* Dordrecht: Springer; 2010. p. 11–22.
- [49] More JJ. The Levenberg Marquardt algorithm: implementation and theory. In: Watson GA, editor. *Lecture notes in Mathematics* vol. 630. New York: Springer-Verlag; 1978. p. 105–116.
- [50] Goerbitz CH. What is the best crystal size for collection of X-ray data? Refinement of the structure of glycyl-L-serine based on data from a very large crystal. *Acta Crystallogr.* 1999;B55:1090–1098.
- [51] Ruehl S, Bolte M. Strategies for data collection on a CCD-diffractometer. *Z Kristallogr.* 2000;215: 499–509.
- [52] Friese K, Grzechnik A, Posse JM, Petricek V. Refinement of high pressure single-crystal diffraction data using Jana 2006. *High Press. Res.* 2013;33:196–201.
- [53] Angel RJ. Absorption corrections for diamond-anvil pressure cells implemented in the software package Absorb 6.0. *J Appl Crystallogr.* 2004;37:486–492.
- [54] He BB. *Two-dimensional X-Ray diffraction.* Hoboken:Wiley; 2009.
- [55] McCarthy AC, Downs RT, Thompson RM. Compressibility trends of the clinopyroxenes, and in-situ high-pressure single-crystal X-ray diffraction study of jadeite. *Am Mineral.* 2008;93:198–209.
- [56] Downs RT, Palmer DC. The pressure behavior of a cristobalite. *Am Mineral.* 1994;79:9–14.
- [57] Kantor A, Kantor I, Merlini M, Glazyrin K, Prescher C, Hanfland M, Dubrovinsky L. High-pressure structural studies of eskolaite by means of single-crystal X-ray diffraction. *Am Mineral.* 2012; 97:1764–1770.